# Instability of the finite-difference split-step method applied to the nonlinear Schrödinger equation. Part I: Standing soliton

T.I. Lakoba*

Department of Mathematics and Statistics, University of Vermont, Burlington, VT 05401, USA

September 30, 2015

**Abstract**

We consider numerical instability that can be observed in simulations of solitons of the nonlinear Schrödinger equation (NLS) by a split-step method where the linear part of the evolution is solved by a finite-difference discretization. The von Neumann analysis predicts that this method is unconditionally stable on the background of a constant-amplitude plane wave. However, simulations show that the method can become unstable on the background of a soliton. We present an analysis explaining this instability. Both this analysis and the features and threshold of the instability are substantially different from those of the Fourier split-step method, which computes the linear part of the NLS by a spectral discretization. For example, the modes responsible for the numerical instability are not similar to plane waves, as for the Fourier split-step method or, more generally, in the von Neumann analysis. Instead, they are localized at the sides of the soliton. This also makes them different from "physical" (as opposed to numerical) unstable modes of nonlinear waves, which (the modes) are localized around the "core" of a solitary wave. Moreover, the instability threshold for the finite-difference split-step method is considerably relaxed compared to that for the Fourier split-step.

**Keywords**: operator splitting; numerical instability; nonlinear evolution equations.

*tlakoba@uvm.edu

# 1 Introduction

The split-step method (SSM), also known as the operator-splitting method, is widely used in numerical simulations of evolutionary equations that arise in diverse areas of science: nonlinear waves, including nonlinear optics and Bose–Einstein condensation [1]–[3], atomic physics [4], and advection–reaction–diffusion equations [5]. In this paper we focus on the SSM applied to the nonlinear Schrödinger equation (NLS):

$$iu_t - \beta u_{xx} + \gamma u|u|^2 = 0. \tag{1.1}$$

Although the real-valued constants $\beta$ and $\gamma$ in (1.1) can be scaled out of the equation, we will keep them in order to distinguish the contributions of the dispersive ($u_{xx}$) and nonlinear ($u|u|^2$) terms. Without loss of generality we will consider $\gamma > 0$ in (1.1); then the sign of $\beta$ determines whether the NLS is of the focusing or defocusing type. Bright solitons exist for the focusing NLS ($\beta < 0$).

The idea of the SSM is that (1.1) can be easily solved analytically when either the dispersive or the nonlinear term is set to zero. This alows one to seek an approximate numerical solution of (1.1) as a sequence of steps which alternatively account for dispersion and nonlinearity:

$$\begin{array}{l} \text{for } n \text{ from 1 to } n_{\max} \text{ do:} \\ \quad \bar{u}(x) = u_n(x)\, \exp\left(i\gamma |u_n(x)|^2 \Delta t\right) \qquad \text{(nonlinear step)} \\ \quad u_{n+1}(x) = \left\{ \begin{array}{l} \text{solution of } \ iu_t = \beta u_{xx} \text{ at } t = \Delta t \\ \text{with initial condition } u(x,0) = \bar{u}(x) \end{array} \right. \qquad \text{(dispersive step)} \end{array} \tag{1.2}$$

where the implementation of the dispersive step will be discussed below. In (1.2), $\Delta t$ is the time step of the numerical integration and $u_n(x) \equiv u(x, n\Delta t)$. Scheme (1.2) can yield a numerical solution of (1.1) whose accuracy is $O(\Delta t)$. Higher-order schemes, yielding more accurate solutions (e.g., with accuracy $O(\Delta t^{\,2})$, $O(\Delta t^{\,4})$, etc.), are known [6, 7, 4], but here we will restrict our attention to the lowest-order scheme (1.2); see also the paragraph after Eq. (3.16) below.

The implementation of the dispersive step in (1.2) depends on the numerical method by which the spatial derivative is computed. In most applications, it is computed by the Fourier spectral method:

$$u_{n+1}(x) = \mathcal{F}^{-1}\left[\, \exp(i\beta k^2 \Delta t)\, \mathcal{F}[\bar{u}(x)] \,\right]. \tag{1.3}$$

Here $\mathcal{F}$ and $\mathcal{F}^{-1}$ are the discrete Fourier transform and its inverse, $k$ is the discrete wavenumber:

$$-\pi/\Delta x \le k \le \pi/\Delta x, \tag{1.4}$$

and $\Delta x$ is the mesh size in $x$. However, the spatial derivative in (1.2) can also be computed by a finite-difference (as opposed to spectral) method [8]–[15]. For example,

using the central-difference discretization of $u_{xx}$ and the Crank–Nicolson method, the dispersion step yields:

$$i\frac{u_{n+1}^m - \bar{u}^m}{\Delta t} = \frac{\beta}{2}\left(\frac{u_{n+1}^{m+1} - 2u_{n+1}^m + u_{n+1}^{m-1}}{\Delta x^{\,2}} + \frac{\bar{u}^{m+1} - 2\bar{u}^m + \bar{u}^{m-1}}{\Delta x^{\,2}}\right), \qquad (1.5)$$

where $u_n^m \equiv u(x_m, n\Delta t)$, $x_m$ is a point in the discretized spatial domain of length $L$: $-L/2 < x_m < L/2$, and $\bar{u}$ is defined in (1.2). Recently, solving the dispersive step of (1.2) by a finite-difference method has found an application in electronic post-processing of optical signals in fiber telecommunications [16].

We will refer to the SSM with spectral (1.3) and finite-difference (1.5) implementations of the dispersive step in (1.2) as s-SSM and fd-SSM, respectively. Our focus in this paper will on the fd-SSM.

In what follows we assume periodic boundary conditions:

$$u(-L/2, t) = u(L/2, t), \qquad u_x(-L/2, t) = u_x(L/2, t). \qquad (1.6)$$

In Sec. 5 we will justify this choice and will also comment on other types of boundary conditions.

Weideman and Herbst [8] used the von Neumann analysis to show that both versions, s- and fd-, of the SSM can become unstable when the background solution of the NLS is a plane wave:

$$u_{\rm pw} = (A/\sqrt{\gamma})\, e^{i\omega_{\rm pw} t}, \qquad A = \text{const}, \quad \omega_{\rm pw} = |A|^2. \qquad (1.7)$$

Specifically, they linearized the SSM equations on the background of (1.7):

$$u_n = u_{\rm pw} + \tilde{u}_n, \qquad |\tilde{u}_n| \ll |u_n| \qquad (1.8)$$

and sought the numerical error in the form

$$\tilde{u}_n = \tilde{A}\, e^{\lambda t_n - ikx}, \qquad \tilde{A} = \text{const}. \qquad (1.9)$$

The SSM is said to be unstable when for a certain wavenumber $k$ one has: (i) $\mathrm{Re}(\lambda) > 0$ in (1.9), but (ii) the corresponding Fourier mode in the original equation (1.1) is linearly stable. Weideman and Herbst found that the s- and fd-SSMs on the background (1.7) become unstable when the step size $\Delta t$ exceeds:

$$\Delta t_{\rm thr,\,s} \approx \Delta x^{\,2}/(\pi|\beta|), \qquad \text{for s-SSM (1.2) \& (1.3)} \qquad (1.10)$$

and

$$\Delta t_{\rm thr,fd} = \Delta x/\sqrt{2|\beta|\gamma\,|A|^2} \quad \underline{\text{only for } \beta > 0}, \qquad \text{for fd-SSM (1.2) \& (1.5)} \qquad (1.11)$$

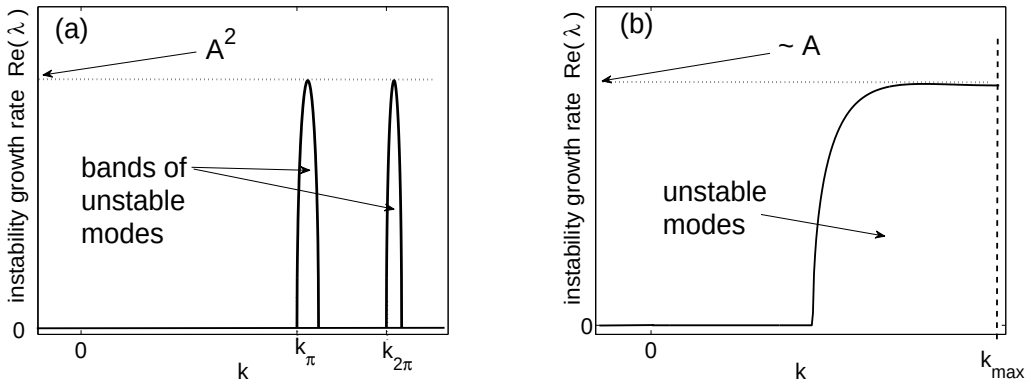


Figure 1: Growth rate of numerical instability of the s-SSM (a) and fd-SSM (b) on the plane-wave background. The dotted horizontal line indicates how the maximum growth rate depends on the wave's amplitude. In (a), $k_{m\pi}$, $m = 1, 2, \ldots$ are the wavenumbers where the $m$th resonance condition holds (see [19]): $|\beta| k_{m\pi}^2 \Delta t = m\pi$.

respectively. Note that for $\beta < 0$, the fd-SSM simulating a solution close to the plane wave (1.7) is unconditionally stable. Typical dependences of the instability growth rate, $\mathrm{Re}(\lambda) > 0$, on the wavenumber is shown in Fig. 1. Let us emphasize that the SSM is unstable for $\Delta t > \Delta t_{\mathrm{thr}}$ even though both its constituent steps, (1.2) and either (1.3) or (1.5), are numerically stable for any $\Delta t$.

Solutions of the NLS (and of other evolution equations) that are of practical interest are considerably more complicated than a constant-amplitude solution (1.7). To analyze stability of a numerical method that is being used to simulate a *spatially varying* solution, one often employs the so-called "principle of frozen coefficients" [17] (see also, e.g., [18]). According to that principle, one assumes some constant value for the solution $u$ and then linearizes the equations of the numerical method to determine the evolution of the numerical error (see (1.8) and (1.9)). However, as we show below, this principle applied to the SSM fails to predict, even qualitatively, important features of the numerical instability (NI).

In this regard we stress — and will subsequently illustrate — that a NI of a particular method applied to a *nonlinear* equation depends, in general, not only on the method and the equation, *but also on the solution which is being simulated*. This is similar to the situation with linear stability analysis of particular solutions of a nonlinear equation: some of those solutions may be stable while others may be not. For example, the plane wave (1.7) of the NLS with $\beta < 0$ is unstable (see, e.g., [2], Sec. 5.1), while the soliton, given by Eq. (1.12) below, is stable with respect to small perturbations of their respective initial profiles.

As a step towards understanding NI on the background of a spatially varying solution,

we analyzed [19] the instability of the s-SSM on the background of a soliton of the NLS:

$$u_{\rm sol}(x,t) = U_{\rm sol}(x)\, e^{i\omega_{\rm sol}t}; \tag{1.12a}$$

$$U_{\rm sol}(x) = A\sqrt{2/\gamma}\,\mathrm{sech}\,(Ax/\sqrt{-\beta}); \qquad \omega_{\rm sol} = A^2. \tag{1.12b}$$

We demonstrated that the instability growth rate in this case is very sensitive to the time step $\Delta t$ and the length $L$ of the spatial domain; also, its dependence on the wavenumber is quite different from that shown in Fig. 1(a). Moreover, the instability on the background of, say, two well-separated (and hence non-interacting) solitons can be completely different from that on the background of one of these solitons. To our knowledge, such features of the NI had not been reported for other numerical methods. In particular, they could not be predicted based on the principle of frozen coefficients. In [19] we showed that all those features could be explained by analyzing a modified linearized NLS satisfied by the numerical error of the s-SSM *with large wavenumber* $k$:

$$i\tilde{v}_t - \omega_{\rm sol}\tilde{v} - \beta(\tilde{v}_{xx} + k_\pi^2\tilde{v}) + \gamma|U_{\rm sol}|^2(2\tilde{v} + \tilde{v}^*) = 0, \tag{1.13}$$

where $\tilde{v}(x,t)$ is proportional to the continuous counterpart of $\tilde{u}_n(x) \equiv \tilde{u}(x, n\Delta t)$ defined similarly to (1.8), and $k_\pi$ is defined in the caption to Fig. 1. Note that (1.13) is similar, but not equivalent, to the NLS linearized about the soliton:

$$i\tilde{u}_t - \omega_{\rm sol}\tilde{u} - \beta\tilde{u}_{xx} + \gamma|U_{\rm sol}|^2(2\tilde{u} + \tilde{u}^*) = 0. \tag{1.14}$$

The extra $k_\pi^2$-term in (1.13) indicates that the potentially unstable numerical error of the s-SSM has a wavenumber close to $k_\pi$.

In this paper we theoretically analyze the NI of the fd- (as opposed to s-) SSM on the soliton background. We will show that, on one hand, the NI of the fd-SSM has a number of distinctly different features both from the NI of the s-SSM and from the textbook examples of NI of linear equations. On the other hand, properties of numerically unstable modes of the fd-SSM are also qualitatively different from properties of physical unstable modes in most known discrete and continuous nonlinear wave equations.

It is an understanding of how these modes "are born" and of their properties that is the main purpose of this study. In such an investigation, it was important to discern and take into consideration only essential features of this problem, at the expense of making the consideration less general. Thus, we have studied a sufficiently simple equation (the pure cubic NLS in one dimension) and its simplest solution — the soliton (1.12) — whose profile $|u(x,t)|$ is not constant in space. As we have noted earlier, properties of NI of a numerical method depend not only on the simulated nonlinear equation, but also on the background solution. Therefore, the NI mechanism that we will reveal here does not have to universally apply to simulations of other solutions of the NLS and/or similar equations. In fact, in subsequent parts of this study, we will analyze NI of a

*moving* (as opposed to standing) soliton of the NLS (in Part II) and of standing and oscillating solitons of the NLS with a bounded potential (in Part III). The NI of a moving soliton will be shown (perhaps surprisingly) to be *completely* different from that of the standing soliton, while the NI in Part III will exhibit *some* differences from the NI considered here. Yet, despite our results being solution-specific, we believe that an important contribution of the present work is in showing a *methodology* of how to analyze NI of various finite-difference numerical methods (not only the fd-SSM), which can be applied to more complicated equations (e.g., the NLS in two or three dimensions).

Our analysis is based on an equation for the large-$k$ numerical error which, as (1.13), is a modified form of the linearized NLS. However, both that equation and its analysis are substantially different from those for the s-SSM [19]. In particular, the modes that render the s- and fd-SSMs unstable are qualitatively different. Namely, for the s-SSM, the numerically unstable modes contain just a few Fourier harmonics and hence are not spatially localized; they resemble plane waves. On the contrary, the modes making the fd-SSM unstable are localized and are supported by the sides (i.e., "tails") of the soliton. To our knowledge, such "tail-supported" localized modes, as opposed to those supported by the soliton's core, have not been reported before in any other system.

The discussion in the previous paragraph is meant to emphasize that we adopt the nonlinear waves community's approach to studying the NI of the SSM. Namely, the numerically unstable modes that we find are just counterparts of unstable modes of solitary waves, except that they occur not due to real physical reasons but due to numerical discretization. By finding those modes, we are also able to estimate a threshold for their instability, as well as their growth rate. Knowing the threshold allows one to take the time step small enough to avoid NI. In addition, knowing the NI growth rate may also be useful because, as we will show in Parts II and III, the NI may be so weak that it does not affect the simulated solution for a long time. In those cases, numerical simulations will produce valid results even if the integration time step exceeds the NI threshold. Using this observation would reduce the computational time.

Our approach should be contrasted with that of the numerical analysis community, where one would focus on obtaining estimates that would guarantee stability for some very broad class (say, localized) solutions of the NLS. Such an approach for a problem similar to the one considered here was used, e.g., in [13]. Its main result will be compared with ours in Sec. 5.

The main part of this manuscript is organized as follows. In Sec. 2 we present simulation results showing the development of NI of the fd-SSM applied to the soliton (1.12). In Sec. 3 we derive an equation (a counterpart of (1.13)) governing the evolution of the numerical error, and in Sec. 4 obtain its localized solutions that grow exponentially in time. Conclusions of our work are summarized in Sec. 5. In Appendices A and B we

discuss technical issues of solving an eigenvalue problem, Eq. (4.2) below. In Appendix C we discuss how the NI sets in.

# 2 Numerical experiments

We simulated Eq. (1.1) with $\beta = -1$, $\gamma = 2$, and the periodic boundary conditions (1.6) via the fd-SSM algorithm (1.2) & (1.5). The domain length was set as $L = 40$ in all simulations reported below. The initial condition was the soliton (1.12) with $A = 1$:

$$u_0(x) = \operatorname{sech}(x) + \xi(x); \tag{2.1}$$

the noise component $\xi(x)$ with zero mean and the standard deviation $10^{-10}$ was added in order to reveal the unstable Fourier components sooner than if they had developed from a round-off error.

Below we report results for two values of the spatial mesh size $\Delta x = L/N$, where $N$ is the number of grid points. We used $N = 2^9$ and $N = 2^{10}$, which yielded $\Delta x \approx 0.078$ and $\Delta x \approx 0.039$, respectively. We verified that, for a fixed $\Delta x$, the growth rate of the NI and parameters of unstable modes, to be described below, are insensitive to the domain's length $L$ (unlike they are for the s-SSM [19]) as long as $L$ is sufficiently large. Also, at least for the selected values of $\Delta x$ in the range $\Delta x \in (0.009,\, 0.078)$ that we have considered, these quantities depend on $\Delta x$ monotonically (again, unlike for the s-SSM).

First, let us remind the reader that the analysis of [8] on a constant-amplitude background (1.7) for $\beta < 0$ predicted that the fd-SSM should be stable for any $\Delta t$.[1] For the soliton initial condition (2.1), which exists also for $\beta < 0$, and for the parameters stated above, our simulations show that the numerical method becomes unstable for $\Delta t > \Delta x$. Clearly, this result could not have been predicted by the method of frozen coefficients.

For future use we introduce a notation:

$$C = (\Delta t/\Delta x)^2 \,. \tag{2.2}$$

In Fig. 2(a) we show the Fourier spectrum of the numerical solution of (1.1), (2.1) obtained by the fd-SSM with $C = 0.95$ (i.e., slightly below the instability threshold) at $t = 100,000$. It shows no trace of NI: the amplitudes of Fourier harmonics beyond the soliton's spectrum remains at the noise floor level. Figure 2(b) shows the spectrum of the numerical solution obtained with $C = 1.05$ (i.e., slightly above the NI threshold) at $t = 800$. The numerically unstable modes are seen near the edges of the spectral axis.

[1] Note that the stability of instability of the numerical method is in no way related to that of the actual solution. In fact, the plane wave (1.7) is modulationally unstable for $\beta < 0$, while it is modulationally stable for $\beta > 0$.

At $t = 1000$, these modes are still small enough so as not to cause visible damage to the soliton: see the solid curve in Fig. 2(c). However, at a later time, the soliton begins to drift: see the dashed line in Fig. 2(c), that shows the numerical solution at $t = 1100$. Such a drift may persist over a long time: e.g., for $C = 1.05$, the soliton still keeps on moving at $t \sim 4000$. However, eventually it gets overcome by noise and loses its identity.

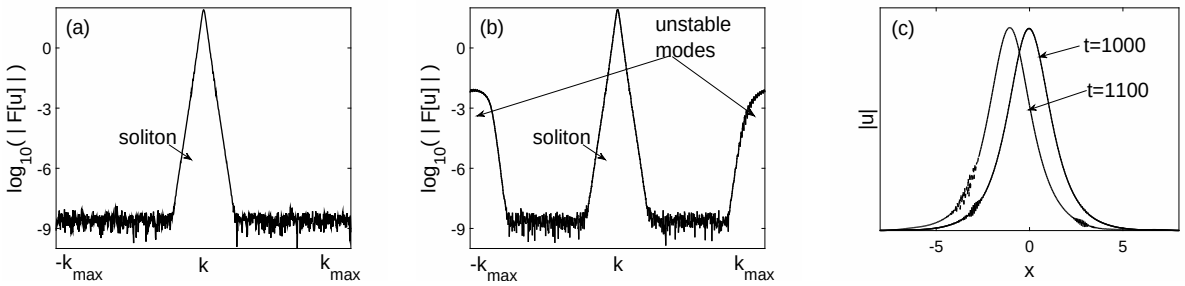


Figure 2: (a), (b): Fourier spectra of the stable (a) and unstable (b) numerical solutions of (1.1) with initial condition (2.1). (c): Effect of numerically unstable modes on the soliton. Details are presented in the text.

We observed the same scenario for several different values of $\Delta x$, $L$, and $C$ (for $C > 1$). The direction of the soliton's drift appears to be determined by the initial noise; this direction is *not* affected by the placement of the initial soliton closer to either boundary of the spatial domain. The time when the drift's onset becomes visible decreases, and the drift's velocity increases, as $C$ increases.

The soliton's drift is a nonlinear stage of the development of the numerical instability and will be explained in Sec. 4.2. In the linear stage, the numerically unstable modes are still small enough so that they do not visibly affect the soliton or one another. To describe this stage, we computed a numeric approximation to the instability growth rate $\mathrm{Re}(\lambda)$ defined in (1.9):

$$\mathrm{Re}\,(\lambda)|_{\mathrm{computed}} = \frac{\ln\left(\begin{array}{c}\max|\mathcal{F}[u](k)| \ \text{ for} \\ k \sim k_{\max} \text{ at time}= t\end{array}\right) - \ln\left(\begin{array}{c}\text{noise floor} \\ \text{at time}= 0\end{array}\right)}{t}, \qquad (2.3)$$

where $k_{\max} = \pi/\Delta x$ (see (1.4)). The so computed values of the instability growth rate are shown in Fig. 3 along with the results of a semi-analytical calculation presented in Sec. 4.1. It is worth pointing out that, especially near the NI threshold, the NI growth rate increases as $\Delta x$ becomes smaller (for a given $C$).

The above numerical results motivate the following three questions: (i) explain the observed instability threshold $\Delta t$ (see the sentence before (2.2)); (ii) identify the modes responsible for the NI; and (iii) calculate the instability growth rate (see Fig. 3). In Sec. 4 we will give an approximate analytical answer to question (i). Answers to questions (ii)

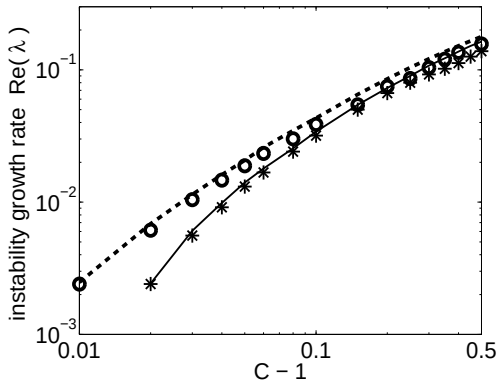


Figure 3: Growth rate of the NI for $\Delta x \approx 0.078$ (solid line — analysis of Sec. 4, stars — computed by (2.3)) and for $\Delta x \approx 0.039$ (dashed line — analysis of Sec. 4, circles — computed by (2.3)).

and (iii) will be obtained only semi-analytically, i.e., via numerical solution of a certain eigenvalue problem.

# 3 Derivation of equation for numerical error

Here we will derive a modified linearized NLS — Eq. (3.15) below — for a small numerical error with a high wavenumber, when the fd-SSM simulates an initial condition close to the soliton, (2.1). This modified equation will be a counterpart of (1.13), which was obtained for the s-SSM in [19]. The key difference between (1.13) and (3.15) occurs due to the following. In view of periodic boundary conditions (1.6), the finite-difference implementation (1.5) of the dispersive step in (1.2) can be written as

$$u_{n+1}(x) = \mathcal{F}^{-1}\left[e^{iP(k)}\,\mathcal{F}\left[\bar{u}(x)\right]\right], \tag{3.1}$$

$$e^{iP(k)} \equiv \frac{1+2i\beta r\sin^2(k\Delta x/2)}{1-2i\beta r\sin^2(k\Delta x/2)} = \exp\left[2i\arctan\big(2\beta r\sin^2(k\Delta x/2)\big)\right], \qquad r=\frac{\Delta t}{\Delta x^{\,2}}, \tag{3.2}$$

where $\mathcal{F}$, $\mathcal{F}^{-1}$ were defined after (1.3). For $|k\Delta x| \ll 1$, the exponent in (3.2) equals that in (1.3). However, for $|k\Delta x| > 1$, they differ substantially: see Fig. 4. It is this difference that leads to the instabilities of the s- and fd-SSMs being qualitatively different.

Using Eqs. (1.2) and (3.1), one can write, similarly to Eq. (3.1) in [19], a linear equation satisfied by a small numerical error $\tilde{u}_n$ of the fd-SSM with an *arbitrary* $k$:

$$\mathcal{F}\left[\tilde{u}_{n+1}\right] = e^{iP(k)}\mathcal{F}\left[e^{i\gamma|u_{\rm b}|^2\Delta t}\big(\tilde{u}_n + i\gamma\Delta t(u_{\rm b}^2\tilde{u}_n^* + |u_{\rm b}|^2\tilde{u}_n)\big)\right]. \tag{3.3}$$

Here $\tilde{u}_n$ is defined similarly to (1.8), with $u_{\rm b}$ being either $u_{\rm pw}$ or $u_{\rm sol}$, depending on the background solution. The exponential growth of $\tilde{u}_n$ can occur only if there is sufficiently

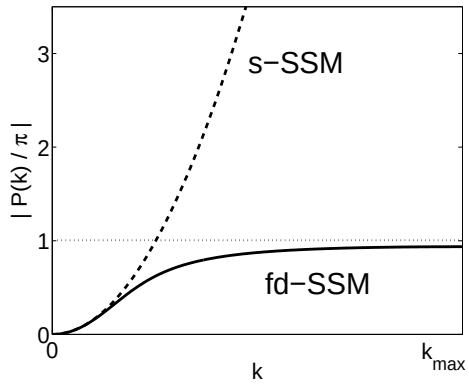


Figure 4: Normalized phase: $|\beta|k^2\Delta t$ for the s-SSM (dashed) and as given by (3.2) for the fd-SSM (solid). In both cases, $r = 5$. The horizontal line indicates the condition of the first resonance: $|P(k)| = \pi$.

strong coupling between $\tilde{u}_n$ and $\tilde{u}_n^*$ in (3.3). This coupling is the strongest when the temporal rate of change of the relative phase between those two terms is minimized. In [19] we showed that this rate can be small only for those $k$ where the exponent $P(k)$ is close to a multiple of $\pi$. Using (3.2) (see also Fig. 4), we see that this can occur only for sufficiently high $k$ where $\sin^2(k\Delta x/2) = O(1)$ rather than $O(\Delta x^2)$. Then, expanding in powers of $(1/r)$, one has:

$$\begin{aligned} -P(k) &= \pi - \frac{1}{|\beta| r \sin^2(k\Delta x/2)} + O\left(\frac{1}{r^3}\right) \\ &= \pi - \frac{1}{|\beta| r} - \frac{(k-k_{\max})^2 \Delta x^2}{4|\beta| r} + O\left(\frac{1}{r^3} + \frac{\big((k-k_{\max})\Delta x\big)^4}{r}\right), \end{aligned} \tag{3.4}$$

where $k_{\max} = \pi/\Delta x$; also recall that $\beta < 0$. We have also used that

$$r = \Delta t/\Delta x^2 = C/\Delta t \gg 1, \tag{3.5}$$

given that the NI was observed in Sec. 2 for $C = O(1)$.

We will now discuss which terms in (3.4) should be retained. First of all, in order to neglect the entire $O$-term, one needs to require that

$$(k-k_{\max})^2 \Delta x^2 \ll O(1), \tag{3.6a}$$

where we have also used (3.5) to neglect the $O(1/r^3)$-term. Next, if we keep the third term on the right-hand side (r.h.s.) of (3.4), it should be greater (in the order of magnitude sense) than the discarded $O$-term, whence

$$(k-k_{\max})^2 \Delta x^2 \gg O(1/r^2) = O(\Delta x^2). \tag{3.6b}$$

It is not particularly important where in the range defined by (3.6a) and (3.6b) the value of $(k-k_{\max})^2\Delta x^2$ should be. For example, if we take it in the middle of that range:

$$|k-k_{\max}| = O(1/\sqrt{\Delta x}). \tag{3.6c}$$

then the three terms on the r.h.s. of (3.4) have orders of magnitude $O(1)$, $O(\Delta x)$, and $O(\Delta x^2)$. What *is* important is that we have chosen to keep the third term in (3.4) and hence required (3.6b). We stress that this choice has followed not from our derivation but rather from our numerical results, as illustrated by Fig. 2(b). Indeed, one sees from that figure that the width of the bands of unstable modes, i.e. $|k-k_{\max}|$, is significantly greater than the spectral width of the soliton, which is of order one. Let us note that in Part II of this study we will encounter a situation where, in contrast to the above, the third term on the r.h.s. of (3.4) will *not* need to be kept. As here, this conclusion will be based on numerics. At present we do not know how to predict the spectral width of unstable bands from analytic considerations taking into account only the form of the background solution.

Substituting the first three terms on the r.h.s. of (3.4) into (3.3), using (3.5), and introducing a new variable

$$\tilde{v}_n = \left(e^{-i\pi}\right)^n \tilde{u}_n = (-1)^n \tilde{u}_n, \tag{3.7}$$

one obtains:

$$\begin{aligned} \mathcal{F}[\tilde{v}_{n+1}] \;\; = \;\; & \exp\left(-\frac{i\Delta t}{C\beta}\left\{1+\frac{(k-k_{\max})^2\Delta x^2}{4}\right\}\right) \times \\ & \mathcal{F}\left[e^{i\gamma|u_{\rm b}|^2\Delta t}\,\left\{\tilde{v}_n + i\gamma\Delta t(u_{\rm b}^2\tilde{v}_n^* + |u_{\rm b}|^2\tilde{v}_n)\right\}\right]. \end{aligned} \tag{3.8}$$

Note that (3.8) describes a *small* change of $\tilde{v}_n$ occurring over the step $\Delta t$, because for $\Delta t \to 0$, the r.h.s. of that equation reduces to $\mathcal{F}[\tilde{v}_n]$. Therefore we can approximate the *difference* equation (3.8) by a *differential* equation, as we will now explain.

First, recall from (3.6a) that the wavenumbers of $\tilde{v}_n$ are on the order of $k_{\max}$; hence we seek[2]

$$\tilde{v}_n(x) = e^{ik_{\max}x}\,\tilde{w}_n(x). \tag{3.9}$$

The effective wavenumber of $\tilde{w}_n$ is then $(k-k_{\max})$, and according to (3.6a) $\tilde{w}_n$ varies slowly over the scale $O(\Delta x)$. Introducing the scaled variables by

$$\chi = x/\epsilon, \quad k_{\rm sc} = (k-k_{\max})\epsilon, \qquad \epsilon = \Delta x/2, \tag{3.10}$$

[2]Strictly speaking, since the spectrum of the numerical error is symmetric relative to $k=0$, as seen from Fig. 2(b), one should have assumed $\tilde{v}_n(x) = \exp[ik_{\max}x]\,\tilde{w}_n^+(x) + \exp[-ik_{\max}x]\,\tilde{w}_n^-(x)$ instead of (3.9). However, both approaches can be shown to lead to the same conclusions and hence here we will use the simpler one based on (3.9).

one rewrites (3.8) as:

$$\mathcal{F}_{\rm sc}[\tilde{w}_{n+1}] = \exp\left(-\frac{i\Delta t}{C\beta}\{1+k_{\rm sc}^2\}\right)\ \mathcal{F}_{\rm sc}\left[e^{i\gamma|u_{\rm b}|^2\Delta t}\ \left\{\tilde{w}_n + i\gamma\Delta t(u_{\rm b}^2\tilde{w}_n^* + |u_{\rm b}|^2\tilde{w}_n)\right\}\right], \tag{3.11}$$

where now $\mathcal{F}_{\rm sc}$ is the Fourier transform with respect to the scaled variables (3.10). In handling the $\tilde{v}_n^*$ term in (3.8), we have used the fact that on the spatial grid $x_m = m\Delta x$, one has:

$$\tilde{v}_n^*(x_m) = e^{-ik_{\max}x_m}\tilde{w}_n^*(x_m) = e^{-i\pi m}\tilde{w}_n^*(x_m) = e^{i\pi m}\tilde{w}_n^*(x_m) = e^{ik_{\max}x_m}\tilde{w}_n^*(x_m).$$

Second, note that the s-SSM (1.2), (1.3) can be written as

$$\mathcal{F}[u_{n+1}] = e^{i\beta k^2\Delta t}\ \mathcal{F}\left[e^{i\gamma|u|^2\Delta t}\,u\right]. \tag{3.12}$$

When $|\beta|k^2\Delta t \ll 1$ and $\gamma|u|^2\Delta t \ll 1$, this is equivalent to the NLS (1.1) *plus* a term proportional to

$$\Delta t\ \left[\beta\partial_x^2,\ \gamma|u|^2\right]_-\,u + O(\Delta t^{\,2}), \tag{3.13}$$

where $[\ldots,\ \ldots]_-$ denotes a commutator (see, e.g., Sec. 2.4 in [2]). Equation (3.11) has the form of a linearized Eq. (3.12) with a different coefficient in the dispersion term and with an extra phase. Therefore, (3.11) must be equivalent[3] to a modified linearized NLS, with the modification affecting only the corresponding terms:

$$i\tilde{w}_t + (\tilde{w}_{\chi\chi} - \tilde{w})/(C\beta) + \gamma(u_{\rm b}^2\tilde{w}^* + 2|u_{\rm b}|^2\tilde{w}) = 0, \tag{3.14}$$

*plus* a $O(\Delta t)$-term proportional to the linearized form of the commutator (3.13). Neglecting that latter term in comparison to the $O(1)$-terms in (3.14) and denoting $\psi = \tilde{w}\ \exp(-i\omega_{\rm b}t)$ to eliminate the explicit time dependence in the $u_{\rm b}^2\tilde{w}^*$-term, we rewrite (3.14) as:

$$i\psi_t + \delta\psi + \psi_{\chi\chi}/(C\beta) + \gamma U_{\rm b}^2(\epsilon\chi)\ (2\psi + \psi^*) = 0, \tag{3.15}$$

where

$$\delta = -\omega_{\rm b} - 1/(C\beta). \tag{3.16}$$

Here $\omega_{\rm b}$ is either $\omega_{\rm pw}$ or $\omega_{\rm sol}$, and $U_{\rm b}$ is either constant or $U_{\rm sol}$, depending on whether the background solution is a plane wave (1.7) or a soliton (1.12). The modified linearized NLS (3.15) for the fd-SSM is the counterpart of Eq. (1.13) that was derived for the s-SSM.

Our subsequent analysis of the instability of the first-order accurate fd-SSM (1.2) & (1.5) will be based on Eq. (3.15). The instability of the second-order accurate version of this method, where the order of the nonlinear and dispersive steps is alternated in any

[3]This was confirmed by direct and tedious Taylor expansion of $\tilde{w}_{n+1}$ in (3.11).

two consecutive full time steps [6], is the same as that of the first-order version. The instability of higher-order versions (e.g., $O(\Delta t^4)$-accurate) can be studied similarly to how that was done in Ref. [19] for the s-SSM.

The boundary conditions satisfied by $\psi$ are still periodic:

$$\psi(-L/(2\epsilon),\, t) = \psi(L/(2\epsilon),\, t), \qquad \psi_\chi(-L/(2\epsilon),\, t) = \psi_\chi(L/(2\epsilon),\, t). \tag{3.17}$$

This follows from the fact that $\tilde{u}_n(x)$ satisfies the periodic boundary conditions (1.6) and from (3.9), given that for $k_{\max} = \pi/\Delta x$ and $L/2 = M\Delta x$ with some integer $M$,

$$e^{-ik_{\max}L/2} = e^{-iM\pi} = e^{iM\pi} = e^{ik_{\max}L/2}.$$

There are three differences between Eq. (3.15) and the linearized NLS (1.14). Most importantly, (3.15) has the opposite sign of the dispersion term. This is explained by the shape of the curve $P(k)$ for the fd-SSM in Fig. 4 at high wavenumbers, where the curvature is opposite to that at $k \approx 0$. Secondly, unlike the $(-\omega_{\rm sol})$-term in (1.14), the $\delta$-term in (3.15) with $\beta < 0$ can be either positive or negative, depending on the value of $C$. Thirdly, the "potential" $U_{\rm b}^2(\epsilon\chi)$ (when $U_{\rm b} \equiv U_{\rm sol}$) is a *slow* function of the scaled variable $\chi$. That is, solutions of (3.15) that vary on the scale $\chi = O(1)$ "see" the soliton as being very wide.

Before proceeding to find unstable modes of Eq. (3.15) with $U_{\rm b} \equiv U_{\rm sol}$, let us note that (3.15) with $U_{\rm b} = {\rm const}$ confirms the result of Ref. [8] regarding the instability of the fd-SSM on the plane-wave background. Namely, for $\beta < 0$, Eq. (3.15) with $U_{\rm b} = {\rm const}$ describes the evolution of a small perturbation to the plane wave in the *modulationally stable* case (see, e.g., Sec. 5.1 in [2]). That is, for $\beta < 0$, there is no NI, in agreement with [8]. On the other hand, for $\beta > 0$, Eq. (3.15) describes the evolution of a small perturbation in the *modulationally unstable* case, and hence the plane wave of the NLS (1.1) can become numerically unstable. The corresponding instability growth rate found from (3.15) and Eq. (5.1.8) of [2] can be shown to agree with the one that can be obtained from Eq. (37) and the next two unnumbered relations in [8]. An example of this growth rate is shown in Fig. 1(b). Also, using our (3.15) and Eq. (5.1.8) of Ref. [2], the threshold value of $\Delta t$ can be shown to be given by (1.11), in agreement with [8].

# 4 Analysis of NI on background of soliton

## 4.1 Unstable modes of modified linearized NLS (3.15)

For the soliton, $U_{\rm b}$ in (3.15) equals $U_{\rm sol}$ given by (1.12). Substituting into (3.15) and its complex conjugate the standard ansatz [20] $(\psi(\chi,t),\, \psi^*(\chi,t)) = (\phi_1(\chi),\, \phi_2(\chi))\, e^{\lambda t}$ and

using yet another rescaling:

$$X = \frac{A}{\sqrt{-\beta}}\chi \equiv \frac{2A}{\sqrt{-\beta}}\frac{x}{\Delta x}, \qquad D = -\frac{C\beta^2}{A^2}\delta \equiv \beta^2\left(\frac{1}{\beta A^2} + C\right), \\ \Lambda = \frac{C\beta^2}{A^2}\lambda, \qquad V(y) = 2C\beta^2 \mathrm{sech}^{\,2}(y), \tag{4.1}$$

one obtains:

$$\left(\partial_X^2 + D - V(\epsilon X)\begin{pmatrix} 2 & 1 \\ 1 & 2 \end{pmatrix}\right)\vec{\phi} = i\Lambda\sigma_3\vec{\phi}, \tag{4.2}$$

where $\sigma_3 = \mathrm{diag}(1, -1)$ is a Pauli matrix, $\vec{\phi} = (\phi_1,\, \phi_2)^T$, and $T$ stands for a transpose. If $(\vec{\phi},\, \Lambda)$ is an eigenpair of (4.2), then so are $(\sigma_1\vec{\phi},\, -\Lambda)$, $(\vec{\phi}^*,\, -\Lambda^*)$, and $(\sigma_1\vec{\phi}^*,\, \Lambda^*)$, where

$$\sigma_1 = \begin{pmatrix} 0 & 1 \\ 1 & 0 \end{pmatrix}$$

is another Pauli matrix. Note also that $\lambda$ is defined in the same way as in (1.9); hence $\mathrm{Re}(\Lambda) \neq 0$ indicates an instability. Below we will use shorthand notations $\Lambda_R = \mathrm{Re}(\Lambda)$ and $\Lambda_I = \mathrm{Im}(\Lambda)$.

We begin analysis of (4.2) with two remarks. First, this equation is qualitatively different from an analogous equation that arises in studies of stability of both bright [20] and dark [21] NLS solitons in that the relative sign of the first and third terms of (4.2) is opposite of that in [20, 21]. This fact is the main reason why the unstable modes supported by (4.2) are qualitatively different from unstable modes of linearized NLS-type equations, as we will see below. While the latter modes are supported by the soliton's core (see, e.g., Fig. 3 in [22]), the unstable modes of (4.2) are supported by the soliton's "tails".

Second, from (4.2) and (4.1) one can easily establish the minimum value of parameter $C$ where an instability (i.e., $\Lambda_R \neq 0$) *can* occur. The matrix operators on both sides of (4.2) are Hermitian; the operator $\sigma_3$ on the r.h.s. is not sign definite. Then the eigenvalues $\Lambda$ are guaranteed to be purely imaginary when the operator on the l.h.s. is sign definite [23]; otherwise they may be complex. The third term on the l.h.s. of (4.2) is negative definite, and so is the first term in view of (3.17). The second term, $D$, is negative when

$$C < 1/(|\beta|A^2). \tag{4.3}$$

Thus, (2.2) and (4.3) yield the stability condition of the fd-SSM on the background of a soliton. We will show later that an unstable mode indeed first arises when $C$ just slightly exceeds the r.h.s. of (4.3).

Since the potential term in (4.2) is a slow function of $X$, it may seem natural to employ the Wentzel–Kramers–Brillouin (WKB) method to analyze it. In Appendix A we show that, unfortunately, the WKB method fails to yield an analytic form of unstable

modes of (4.2). Yet, as we also show there, it allows one to predict that localized modes of (4.2) cannot exist around the soliton's core and thus may only exist at the soliton's sides.

In Fig. 5 we show the first (i.e., corresponding to the greatest $\Lambda_R$) such a mode for $L = 40$, $N = 2^9$ points (hence $\epsilon = \Delta x/2 \approx 0.04$), $A = 1$, $\beta = -1$, $\gamma = 2$. For these parameters, the threshold given by the r.h.s. of (4.3) is $C = 1$, and parameter $D$ in (4.2) is related to $C$ by:

$$D = C - 1. \tag{4.4}$$

The numerical method of solving (4.2) is described in Appendix B, and the modes found by this method are shown in Fig. 5(a) for different values of $C$. In Fig. 5(b) we show the same modes obtained from the numerical solution of the NLS (1.1) by the fd-SSM. These modes were extracted from the numerical solution by a high-pass filter, and then the highest-frequency harmonic was factored out as per (3.9). The agreement between Figs. 5(a) and 5(b) is seen to be good. Note that Fig. 5 shows, essentially, the envelope of the unstable mode. The mode *not extracted* from the numerical solution is shown in Fig. 6(a); it can also be seen at the "tails" of the soliton in Fig. 2(c).

In Fig. 6(b) we show the location of the peak of the envelope of the first unstable mode, computed both from (4.2) and from the numerical solution of (1.1), versus parameter $C$. The corresponding values of the instability growth rate $\lambda$ were shown earlier in Fig. 3. Let us stress that $\lambda$ for the localized modes of (4.2) was found to be purely real up to the computer's round-off error ($\sim 10^{-15}$). There also exist unstable modes with complex $\lambda$, but such modes were found to be not localized and to have smaller growth rates than the localized modes.

As $C$ increases from the critical value given by (4.3), the localized unstable mode becomes narrower and also moves toward the center of the soliton. Moreover, higher-order localized modes of (4.2) arise. Typical profiles of the second and third modes are shown in Fig. 7, along with the parameter $C$ for which such modes first become localized within the spatial domain. In Appendix C we demonstrate that the process of "birth" of an eigenmode that eventually (i.e., with the increase of $C$) becomes localized, is rather complicated. In particular, it is difficult to pinpoint the exact value of parameter $C$ where such a mode appears. Therefore, the $C$ values shown in Fig. 7 are accurate only up to the second decimal place.

## 4.2 Effect of unstable modes on soliton

Let us now show how our results can qualitatively explain the observed dynamics of the numerically unstable soliton — see the text after Eq. (2.2) and Fig. 2(c). Let $\tilde{u}_{\text{unst}}$ be

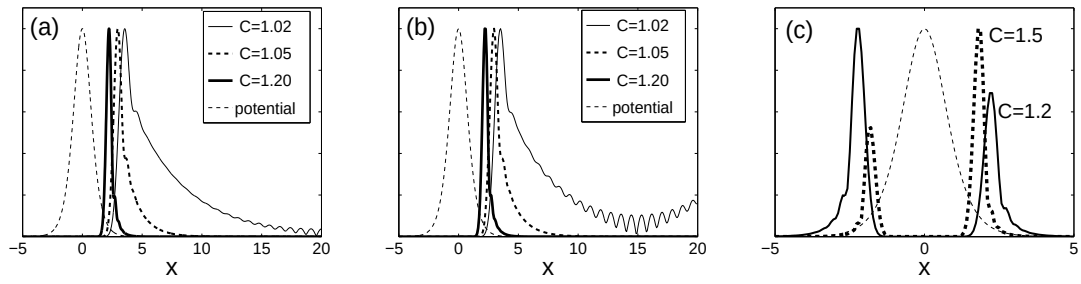


Figure 5: (a) Envelopes of the first localized mode on the right side of the soliton for different values of $C$, as found by the numerical method of Appendix B. (b) Same as in (a), but found from the numerical solution of (1.1), as explained in the text. (c) The modes at *both* sides of the soliton found from the numerical solution of (1.1). Note that these modes do not "see" each other because of the barrier created by the soliton, and hence in general have different amplitudes as they develop from independent noise seeds. In all panels, the potential is $\mathrm{sech}^2(\epsilon X)$ (see (4.1)) and the amplitude of the mode is normalized to that of the potential.

the field of the unstable modes at the soliton's sides. At an early stage of the instabilty, it is much less than the amplitude of the soliton: $|\tilde{u}_{\rm unst}| \ll A$. Also, its characteristic wavenumbers are much greater than those of the soliton: see Fig. 2(b) and (3.6). Then, to determine its effect on the soliton, one substitutes $u = u_{\rm sol} + u_{\rm unst}$ into the NLS (1.1) and discards all the high-wavenumber terms to obtain:

$$i(u_{\rm sol})_t - \beta(u_{\rm sol})_{xx} + \gamma u_{\rm sol}|u_{\rm sol}|^2 = -2\gamma u_{\rm sol}|u_{\rm unst}|^2. \tag{4.5}$$

This is the equation for a perturbed soliton with the perturbation being, in general, not symmetric about the soliton's center (see Fig. 5(c)). Indeed, the modes on the left and right sides of the soliton do not "see" each other through the wide barrier created by the soliton's core and hence can have different amplitudes. Such an asymmetric perturbation is known (see, e.g., [2], Sec. 5.4.1) to cause the soliton to move, which is precisely the effect reported in Fig. 2(c).

# 5 Conclusions

The main contribution of this work is the development of the (in)stability analysis of the fd-SSM beyond the von Neumann (i.e., constant-coefficient) approximation. As previously for the s-SSM [19], our analysis is based on a modified equation for the Fourier modes of the numerical error that approximately satisfy the resonance condition

$$|\beta|k^2\Delta t = \pi. \tag{5.1}$$

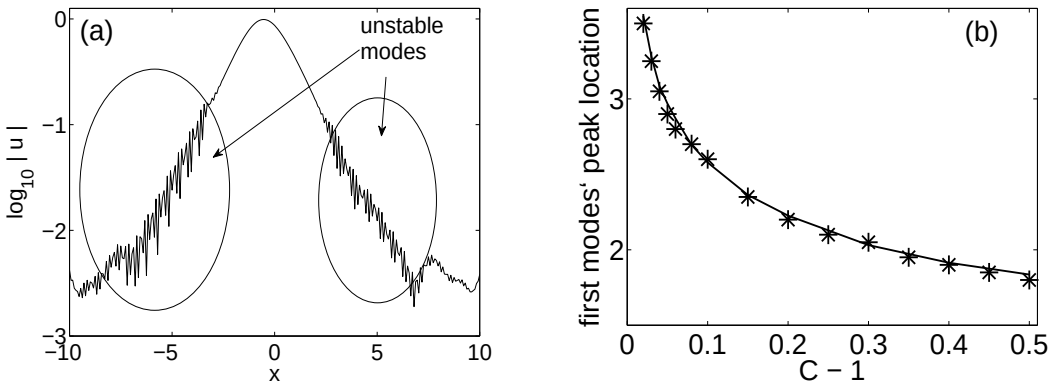


Figure 6: (a) The numerical solution for $t = 1500$ and the same parameters as in Fig. 5, with $C = 1.05$. (b) Location of the peak of the envelope of the first localized mode, found by the method of Appendix B (solid line) and from the solution of (1.1) (stars). Similar data for $L = 40$ and $N = 2^{10}$ are very close and hence are not shown.

Analyzing the (in)stability of the fd-SSM then proceeds similarly to the (in)stability analysis of nonlinear waves, i.e., by solving an eigenvalue problem with a spatially-varying potential. In view of this it is clear that properties of NI and, in particular, its threshold, depend on the simulated solution and thus cannot be expected to be universally applicable to all solutions. In this part of our study, we explained the mechanism and generic features of the NI for the standing soliton of the NLS.

The modified equation for the numerical error, Eq. (3.15), is different from the analogous modified equation, (1.13), for the s-SSM. Their analyses are also qualitatively different, and so are the modes that are found to cause the instability of these two numerical methods. For the s-SSM, these modes are almost monochromatic (i.e., non-localized) waves $\sim \exp(\pm ikx)$ that "pass" through the soliton very quickly. It is this scattering of those waves on the soliton that was shown [19] to lead to their instability. In contrast, for the fd-SSM considered in this work, the dominant unstable modes are stationary relative to the soliton. Moreover, they are localized *at the sides*, as opposed to the core, of the soliton. To our knowledge, such localized modes were not reported before in studies of instability of nonlinear waves.

Since both the soliton and the unstable modes are localized, it is intuitively clear that using boundary conditions other than periodic ones, (1.6), should not affect the NI. We have verified and confirmed this for zero Dirichlet boundary conditions.

Equation (4.3) provides an approximate threshold of the NI, and our simulations, reported in Sec. 2 and Appendix C, confirmed that an NI does indeed occur just slightly above it. According to (4.3) and (2.2), our threshold yields the following relation between

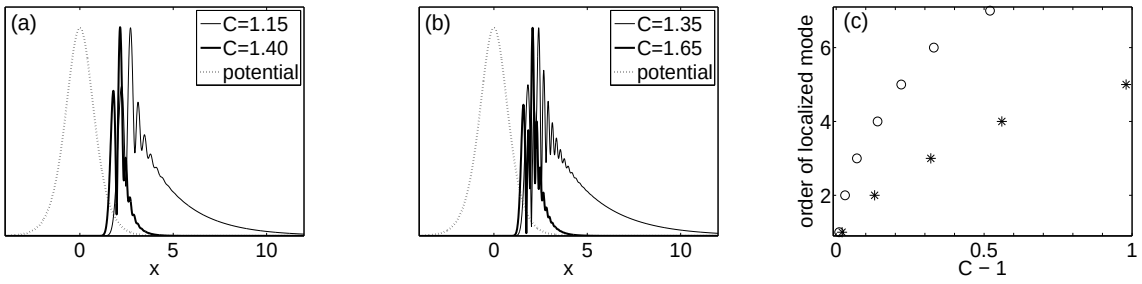


Figure 7: Similar to Fig. 5(a), but for the second (a) and third (b) localized modes. (c): $C$ values where localized modes of increasing order appear. Stars — for $\epsilon = 40/1024$, circles — for $\epsilon = 40/2048$.

the time step and spatial mesh size: $\Delta t = O(\Delta x)$. Recently, a qualitatively different NI threshold was established in [13] (see Eq. (2.9) there) by a different method, yielding $\Delta t = O(\Delta x^2)$. Clearly, our threshold is sharper. However, both analyses, that of [13] and ours, have limitations, which we will briefly discuss below.

The limitation of our analysis is that it is strictly valid only when the initial condition is infinitesimally close to the soliton. In particular, this implies that it is also strictly valid only in the limit $\Delta x \to 0$, because it is only then that the discretization error of the fd-SSM is infinitesimally small.[4] We verified this conclusion by simulating the initial condition (2.1) for $C = 0.99$ (i.e. for $\Delta t$ being 0.5% below the threshold (4.3)) up to $t = 100,000$. The parameters were the same as in Sec. 2, except that we repeated the simulations for $N = 2^{10}$ and $2^{11}$. Note that reducing $\Delta x = L/N$ by the factor of 2 reduces the discretization error, mostly caused by the Crank–Nicolson scheme (1.5), by the factor of 4. For $N = 2^{10}$ ($\Delta x \approx 0.039$), numerically unstable modes became discernible above the noise floor[5] around $t = 50,000$ and have grown by one order of magnitude by $t = 100,000$. (The result of a similar experiment for $C = 0.95$ is shown in Fig. 2(a), where no NI is visible.) For $N = 2^{11}$ ($\Delta x \approx 0.019$), no trace of NI appears at $t = 100,000$.

In contrast, the analysis of [13] does not require the initial deviation from the soliton to be infinitesimally small. (However, it makes a restrictive assumption of it being an even function: $\tilde{u}(-x) = \tilde{u}(x)$.) The price that one pays for removing that requirement

[4] A small but finite discretization error may cause NI in an indirect way, as follows. It will interact with the soliton and cause its oscillations (which may be almost indiscernible); in Part III of this study we will show that NI of an oscillating soliton is manifested somewhat differently from that of the exact stationary soliton. We emphasize that a discretization error would *not* cause NI directly because its spectral content is similar to that of the soliton and hence has only infinitesimally small amount of high-$k$ harmonics, which are the only ones that can become unstable.

[5] An explanation of this delayed appearance of NI will be presented in Parts II and III of this study.

is that the corresponding threshold, $\Delta t = O(\Delta x^2)$, is too conservative. A detailed study of the NI threshold for initial conditions that are not infinitesimally close to the soliton, and also for a generalized NLS, will be presented in Part III of this study.


## Acknowledgement

I thank Jake Williams for help with numerical simulations at an early stage of this work, and Eduard Kirr for a useful discussion. This research was supported in part by NSF grants ECCS-0925706 and DMS-1217006.


## Appendix A: Eq. (4.2) not amenable to WKB, yet qualitatively predicts localized modes at soliton's sides

Away from "turning points" (see below) the WKB-type solution of (4.2) is:

$$\vec{\phi} = \left(a_+ e^{\theta_+/\epsilon} + b_+ e^{-\theta_+/\epsilon}\right)\, \vec{\varphi}_+ + \left(a_- e^{\theta_-/\epsilon} + b_- e^{-\theta_-/\epsilon}\right)\, \vec{\varphi}_-, \tag{A.1}$$

where $a_\pm$, $b_\pm$ are some constants, and

$$(\theta'_\pm)^2 = -D + 2V \pm \sqrt{V^2 - \Lambda^2}, \qquad V \equiv V(\epsilon X), \;\; \theta' \equiv d\theta/d(\epsilon X), \tag{A.2a}$$

$$\vec{\varphi}_\pm = \frac{1}{[(\theta'_\pm)^2 (V^2 - \Lambda^2)]^{1/4}} \begin{pmatrix} \sqrt{\Lambda \pm \sqrt{\Lambda^2 - V^2}} \\ -i\sqrt{\Lambda \mp \sqrt{\Lambda^2 - V^2}} \end{pmatrix}. \tag{A.2b}$$

At a turning point, say, $X = X_0$, the solution (A.1), (A.2) breaks down, which can occur because the denominator in (A.2b) vanishes. In such a case, one needs to obtain a solution of (4.2) in a transition region around the turning point by expanding the potential: $V(\epsilon X) = V(\epsilon X_0) + \epsilon(X - X_0)\, V'(\epsilon X_0) + \ldots$, and then solving the resulting approximate equation. For a single linear Schrödinger equation, a well-known solution of this type is given by the Airy function. This solution is used to "connect" the so far arbitrary constants $a_\pm$, $b_\pm$ in (A.1) on both sides of the turning point.

Now a turning point of (4.2) is where: either (i) $\theta'_+ = 0$ or $\theta'_- = 0$, or (ii) $(V(\epsilon X))^2 - \Lambda^2 = 0$. The former case can be shown (see, e.g., [24]) to reduce to the single Schrödinger equation case, where the solution in the transition region is given by the Airy function. However, at present, no such transitional solution is analytically available in case (ii)[6] [25, 26]. Therefore, the solutions (A.1) canot be "connected" by an analytic formula across such a turning point, and hence one cannot find the eigenpairs $(\vec{\phi}, \Lambda)$ analytically.

Let us now show that if solutions (A.1) are localized, as we expect of unstable modes, then they cannot exist at the soliton's core and thus may only exist at its sides. Indeed,

[6] Note that in this case, $(V^2 - \Lambda^2)^{1/4}\vec{\varphi}_+$ and $(V^2 - \Lambda^2)^{1/4}\vec{\varphi}_-$ are linearly dependent.

assume, for simplicity, that $\Lambda_R \neq 0$ and $\Lambda_I = 0$ for a localized mode (the same conclusion as below can also be reached for $\Lambda_I \neq 0$). Note that just above the instability threshold, $D$ is small (see (4.1) and (4.3)), and so is $\Lambda$. Now, near the soliton's core, $V(\epsilon X) = O(1)$, and hence from (A.2a) one sees that there $\theta_\pm^2 > 0$. Thus, both $\theta_\pm$ are real, and hence the corresponding (A.1) would grow exponentially away from the soliton's core. This, however, is not possible because on the scale of Eq. (4.2), the soliton is very wide, and then a mode growing away from its center would become exponentially large before it reaches the turning point. Thus, the only possibility for a localized mode of (4.2) is to be centered at some point at the soliton's side and decay in both directions away from that point. A straightforward but tedious analysis shows that this is indeed possible when $D > 0$ and $\Lambda_R \neq 0$, and is confirmed by Fig. 5.

# Appendix B: Numerical solution of eigenproblem (4.2)

We multiply both sides of (4.2) by $\sigma_3$ and discretize it using Numerov's method, which approximates the equation $\Phi_{XX} = F(\Phi, X)$ by a finite-difference scheme

$$\Phi^{m+1} - 2\Phi^m + \Phi^{m-1} = \frac{\Delta X^{\,2}}{12}\big(F^{m+1} + 10F^m + F^{m-1}\big) \tag{B.1}$$

with accuracy $O(\Delta X^{\,4})$. Here $\Phi^m \equiv \Phi(X_m)$, $F^m \equiv F(\Phi^m, X_m)$, etc., and $X_m$ are points in the $X$-, not $x$-, domain, with $m = 1, \ldots, M-1$. Note that the number of grid points, $M$, in the $X$-domain is much greater than the number of grid points, $N$, in the $x$-domain, because $X \propto x/\epsilon$; see (4.1), (3.10). Then, for the discretized solution $\mathbf{f}_k = [\phi_k^1, \ldots, \phi_k^{M-1}]^T$ $(k = 1, 2)$ one obtains:

$$(-1)^{k-1}\left(\left[\frac{1}{\Delta X^{\,2}}\mathcal{A} + \mathcal{N}\,\{D\mathcal{I} - 2\mathcal{V}\}\right]\mathbf{f}_k \,-\, \mathcal{N}\,\mathcal{V}\,\mathbf{f}_{3-k}\right) \,=\, i\Lambda\mathcal{N}\,\mathbf{f}_k. \tag{B.2}$$

Here all matrices, denoted by script letters, have size $(M-1)\times(M-1)$: $\mathcal{I}$ is the identity matrix; $\mathcal{A}$ is a circulant matrix with $(-2)$ on the main diagonal, $(+1)$ on the sub- and super-diagonals and in the corner (i.e., $(1, M-1)$th and $(M-1, 1)$th) entries, and the rest of the entries being zero; $\mathcal{N}$ has a similar structure to $\mathcal{A}$ with $\mathcal{N}_{m,m} = 10/12$ (see (B.1)), $\mathcal{N}_{(m-1),m} = \mathcal{N}_{m,(m-1)} = 1/12$, $\mathcal{N}_{1,(M-1)} = \mathcal{N}_{(M-1),1} = 1/12$; and $\mathcal{V} = \mathrm{diag}(V^1, \ldots, V^{M-1})$. Next, defining the combined vector and matrices:

$$\hat{\mathbf{f}} = \begin{bmatrix} \mathbf{f}_1 \\ \mathbf{f}_2 \end{bmatrix}, \quad \hat{\mathcal{A}} = \begin{pmatrix} \mathcal{A} & \mathcal{O} \\ \mathcal{O} & \mathcal{A} \end{pmatrix}, \quad \hat{\mathcal{N}} = \begin{pmatrix} \mathcal{N} & \mathcal{O} \\ \mathcal{O} & \mathcal{N} \end{pmatrix},$$

$$\hat{\mathcal{V}} = \begin{pmatrix} 2\mathcal{V} & \mathcal{V} \\ \mathcal{V} & 2\mathcal{V} \end{pmatrix}, \quad \hat{\sigma}_3 = \begin{pmatrix} \mathcal{I} & \mathcal{O} \\ \mathcal{O} & -\mathcal{I} \end{pmatrix},$$

where $\mathcal{O}$ is the $(M-1)\times(M-1)$ zero matrix, one rewrites (B.2) as:

$$\hat{\sigma}_3\left[\frac{1}{\Delta X^{\,2}}\hat{\mathcal{A}}+D\hat{\mathcal{N}}-\hat{\mathcal{N}}\hat{\mathcal{V}}\right]\hat{\mathbf{f}}\;=\;i\Lambda\hat{\mathcal{N}}\hat{\mathbf{f}}\,. \tag{B.3}$$

This equation has the form of the generalized eigenvalue problem $\mathcal{G}\hat{\mathbf{f}}=\lambda\mathcal{H}\hat{\mathbf{f}}$ where $\mathcal{H}=\hat{\mathcal{N}}$ is a positive definite matrix. This problem can be solved by Matlab's command `eigs`. As its options, we specified that 108 smallest-magnitude eigenvalues and the corresponding eigenmodes needed to be computed. Among them, we looked only at those with complex $\Lambda$. Beyond the instability threshold there are several such modes. We visually inspected them and found that the most unstable mode was also the most localized and also had a real eigenvalue. Finally, we verified that the eigenvalues did not change to five significant figures whether we used $\Delta X=1/10$ or $1/20$; so we used $\Delta X=1/10$.

# Appendix C: "Birth" of localized unstable mode

The NI growth rates plotted in Fig. 3 are monotonic functions of the parameter $C$. This, however, occurs only when $C$ is sufficiently beyond the threshold value given by (4.3). Here we will focus on the evolution of eigenvalues with $\Lambda_R\neq 0$ very close to that threshold. We will show that "birth" of a localized unstable mode occurs in two main stages. First, there is a stage where one or several modes with complex or even purely real eigenvalues appear and disappear as $C$ is increased. These modes are not localized. Then, past some value which we denote $C_{\rm cr}$, a mode with a real $\Lambda>0$ is "born", and its eigenvalue quickly (in $C$) becomes dominant, i.e., begins to significantly exceed real parts of all other eigenvalues *except* one (which is "born" slightly later). Once the dominance of this pair of eigenvalues occurs, their modes become localized. It is these modes (which almost coincide for suffiently large $C-C_{\rm cr}$; see below) that are shown in Fig. 5.

This two-stage process is quite different from a single bifurcation that typically takes place when an unstable mode of a nonlinear wave is "born" (see, e.g., [27]). Our analysis may suggest that this difference results from the finite length, $L$, of our domain, and thus details of the instability development may be similar to those for a breather on a finite lattice [28]. However, a thorough understanding of this issue remains an open problem.

Results presented below are for $L=40$, $N=2^9$ (i.e., $\epsilon=40/1024\approx 0.04$); the rest of parameters is the same as listed in Sec. 2. Parameters $C$ and $D$ are then related by (4.4): $D=C-1$. By solving (4.2) numerically as described in Appendix B, we observed that eigenmodes with $\Lambda_R\neq 0$ are "born" in two ways. One is when two imaginary eigenvalues $\pm i\Lambda_I$ "collide" at the origin (i.e., $\Lambda_I\to 0$) and thereby give rise to two real ones. The

other way is a "collision" of two imaginary eigenvalues $i\Lambda_{I1}$ and $i\Lambda_{I2}$ away from the origin (i.e., $i\Lambda_{I1} \to i\Lambda_{I2} \neq 0$). In that case two complex eigenvalues are "born".[7] The very first (i.e., for the smallest $C$) unstable mode is created in the former way. We will now show that this mode is essentially non-localized and, moreover, it is *not* the mode that eventually becomes the dominant unstable mode. However, to partially understand creation of the latter mode at $C_{\rm cr}$, we need to first discuss the former one.

This earliest, non-localized, mode is created from $\Lambda = 0$. Indeed, for $\Lambda = 0$, Eq. (4.2) can be split into two uncoupled linear Schrödinger equations:

$$\big(\,\partial_X^2 + D - \nu_\pm\, V(\epsilon X)\,\big)\phi_\pm = 0, \qquad \phi_\pm = \phi_1 \pm \phi_2, \tag{C.1a}$$

where $\nu_- = 1$ and $\nu_+ = 3$. Note that, as per (3.17), $\phi_\pm$ satisfy the periodic boundary conditions:

$$\phi_\pm(-L/(2\epsilon)) \;=\; \phi_\pm(L/(2\epsilon)). \tag{C.1b}$$

In Fig. 8(a) we show an example of a nontrivial solution of (C.1). In view of the periodic boundary conditions, this figure is equivalent to Fig. 8(b). Recall from Sec. 4 that the eigenmode is exponentially small inside the soliton. Then the solution shown in Fig. 8(b) can be thought of as being localized inside the valley bounded by the two "halves" of the potential. Using this observation, one can estimate the isolated values of $D$ for which one of the equations (C.1a), along with (C.1b), has a nontrivial solution, by the standard WKB method. The condition for the existence of a mode localized inside the valley of Fig. 8(b) is given by the Bohr–Sommerfeld formula:

$$\left(\int_{-L/(2\epsilon)}^{X_{\rm left}} + \int_{X_{\rm right}}^{L/(2\epsilon)}\right) \sqrt{D - \nu V(\epsilon X)}\, dX \;=\; \pi\left(n + \frac{1}{2}\right), \tag{C.2}$$

where $\nu$ is either $\nu_-$ or $\nu_+$, $n$ is an integer, and $X_{\rm left,\,right}$ are the turning points (see Appendix A), where

$$D - \nu V(\epsilon X_{\rm left,\,right}) = 0. \tag{C.3}$$

The number of full oscillation periods of the mode inside the valley equals $n$; for example, in Fig. 8, $n = 3$.

When $D \ll 1$, the potential in (C.3) can be approximated by an exponential: $\operatorname{sech}^2(\epsilon X) \approx 4\exp(-2\epsilon X)$. Then, using (4.1) and (C.3), we reduce (C.2) to

$$\sqrt{D}\int_{X_{\rm right}}^{L/(2\epsilon)} \sqrt{1 - \exp[-2\epsilon(X - X_{\rm right})]}\, dX \;=\; \frac{\pi}{2}\left(n + \frac{1}{2}\right), \tag{C.4}$$

with $X_{\rm left} = -X_{\rm right}$ and

$$X_{\rm right} = \frac{1}{2\epsilon}\,\ln\frac{8\nu C\beta^2}{D}\,. \tag{C.5}$$

[7] As per the remark after (4.2), there is also a pair of eigenvalues with $(-\Lambda_I)$, so a quadruplet of complex eigenvalues actually appears.

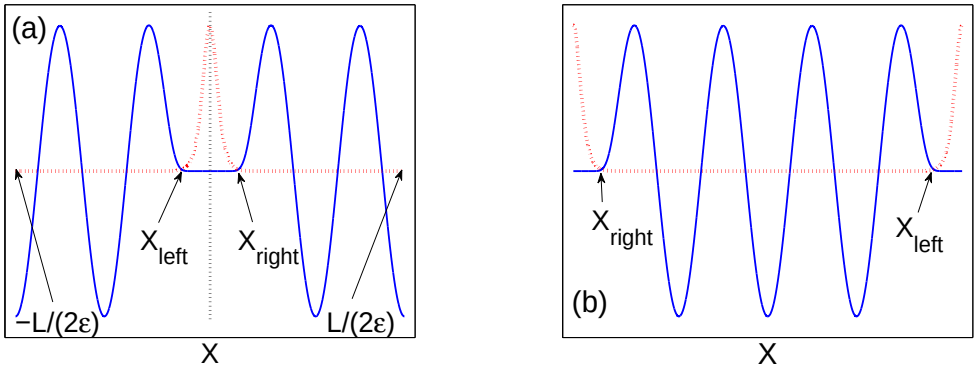


Figure 8: (Color online) (a): A solution of (C.1) (solid); potential $\mathrm{sech}^2(\epsilon X)$ (red dotted). The amplitude of the solution is normalized to that of the potential. (b): Same as (a), but that panel is "cut" along the vertical dotted line at the center, and the resulting halves are interchanged.

Neglecting the exponentially small terms of the order $O\big(\exp[-(L-2\epsilon X_{\rm right})]\big)$, one obtains from (C.4):

$$\sqrt{D}\left(L-\ln\frac{8\nu C\beta^2}{D}-2(1-\ln 2)\right)=\epsilon\,\pi\left(n+\frac{1}{2}\right). \tag{C.6}$$

Note that the WKB condition (C.2), and hence (C.6), is valid when $n$ is sufficiently large. In particular, it is *not* supposed to accurately predict the "birth" of the first unstable mode, where $n=0$. Indeed, Eq. (C.6) predicts that such a mode (for $\nu=1$) emerges at $D\approx 5.9\cdot 10^{-6}$, while numerically it is found at $D\approx 1.6\cdot 10^{-5}$. (A similar mode for $\nu=3$ emerges at a slightly higher value of $D$.) Formula (C.6) becomes accurate to the fourth significant figure in $D$ for $n\gtrsim 20$.

As we noted above, the first unstable mode is *not* the one that eventually becomes the dominant unstable mode. It disappears already at $D\approx 1.7\cdot 10^{-5}$, and there is an adjacent interval of $D$ values where all the eigenvalues of (4.2) are purely imaginary (i.e., the soliton is numerically stable). As $D$ increases, higher-order "real" (i.e., with $\Lambda_I=0$) modes appear and disappear in a similar fashion, as do quadruplets of modes with complex $\Lambda$. In both these types of modes, $\Lambda_R$ is fairly small: $|\Lambda_R|\lesssim D/10$. There also exist intervals of $D$, of increasingly small length, where all $\Lambda$'s are purely imaginary. This situation persists until the dominant unstable mode appears at $D_{\rm cr}\,(=C_{\rm cr}-1)$. This occurs as follows.

First, at $D\approx 0.012134$, a "real" mode appears (see Fig. 9(a,b)), and from this point on there always exists a "real" mode, even though the particular mode "born" at $D\approx 0.012134$ disappears later on. Specifically, at $D\approx 0.012928$, another "real" mode acquires $\Lambda_R$ greater than that of the mode "born" at $D\approx 0.012134$, and the

latter mode soon disappears (Fig. 9(c,d)). A similar switchover between "real" modes occurs at least one more time near $D \approx 0.013750$ (not shown). Next, another "real" mode is "born" via a cascade of bifurcations near $D \approx 0.0162$ (Fig. 9(e,f)), and its $\Lambda_R$ crosses that of the previously dominant-$\Lambda_R$ "real" mode near $D \approx 0.01635$. At $D = 0.0170$, these two dominant "real" modes have $\Lambda_R \approx 1.4 \cdot 10^{-3}$ and $1.5 \cdot 10^{-3}$ (Fig. 9(e)). Finally, these two modes gradually approach each other while crossing at least once more near $D = 0.01725$. At $D = 0.023$ and beyond, their eigenvalues are the same to five significant figures. Thus, remarkably, the dominant unstable mode eventually becomes doubly degenerate. We verified that such a degeneracy also occurs for the higher-order localized unstable modes, shown in Fig. 7.

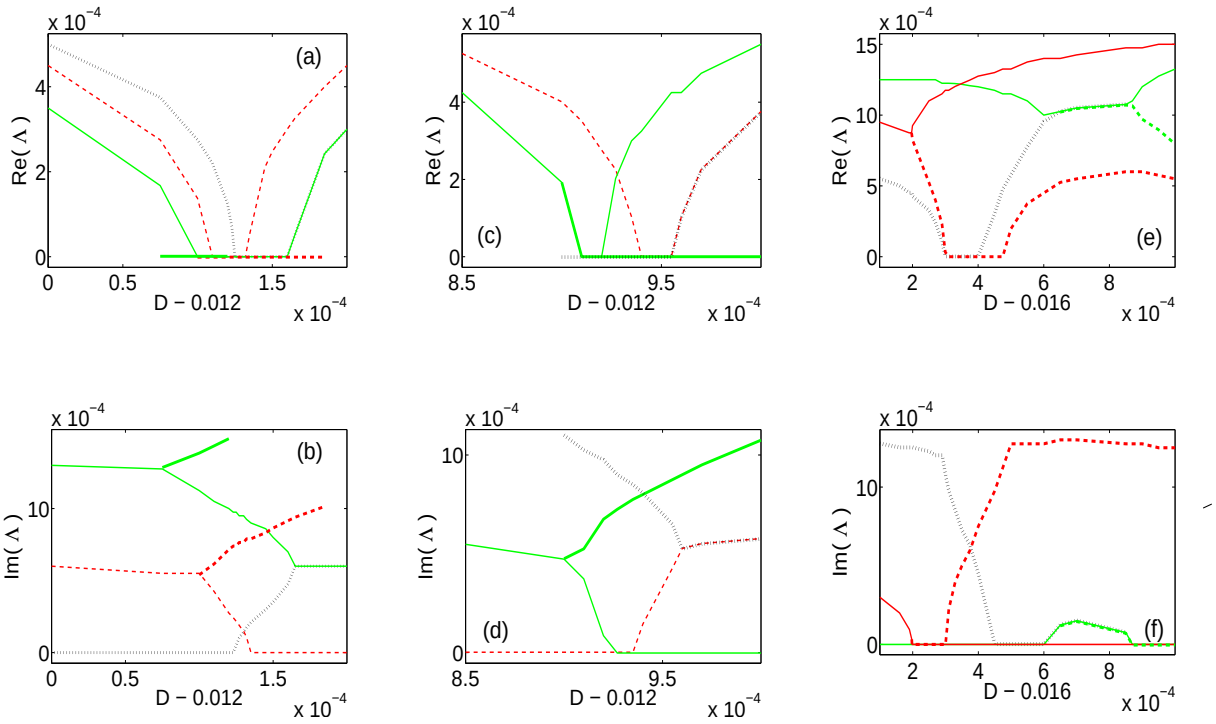


Figure 9: (Color online) Real and imaginary parts of selected modes of (4.2), including the most unstable mode. (a) & (b): $0.01200 \le D \le 0.01220$; (c) & (d): $0.01285 \le D \le 0.01300$; (e) & (f): $0.01610 \le D \le 0.01700$. Same line colors, styles, and widths are used to indicate the same modes within one pair of panels (e.g., (c) & (d)). The same line colors/styles/widths in different pairs of panels (e.g., in (a) & (b) and (c) & (d)) do *not* imply the same modes.

To conclude, we present a hypothesis as to why the value $C_{\rm cr}$, where a "real" mode appears permanently (see above), is near $C = 1.013$. Let us interpret (C.6) in a way that the $n$ on its r.h.s. is not necessarily an integer, but a continuous function of the parameter $D$. For those values of $D$ when $n$ *is* an integer, a mode with a real $\Lambda$ either

appears or disappears at the origin $\Lambda = 0$. Evaluating $n$ at the values of $D$ listed in the previous paragraph in connection with Figs. 9(a)–(d), one finds:

$$\underline{\text{at } D = 0.012134}: \quad n|_{\nu=1} \approx 29.02, \qquad n|_{\nu=1} - n|_{\nu=3} \approx 0.99; \tag{C.7a}$$

$$\underline{\text{at } D = 0.012928}: \quad n|_{\nu=1} \approx 30.02, \qquad n|_{\nu=1} - n|_{\nu=3} \approx 1.02; \tag{C.7b}$$

$$\underline{\text{at } D = 0.013750}: \quad n|_{\nu=1} \approx 31.04, \qquad n|_{\nu=1} - n|_{\nu=3} \approx 1.05. \tag{C.7c}$$

That is, both $n|_{\nu=1}$ and $n|_{\nu=3}$ are simultaneously very close to integers. At $D = 0.012928$, one of the "real" modes has not yet disappeared while the next one has appeared (Fig. 9(c)). From (C.7) we observe that at this value of $D$, the difference $(n|_{\nu=1} - n|_{\nu=3})$ exceeds 1 for the first time. Thus, we hypothesize that $C_{\rm cr} \equiv 1 + D_{\rm cr}$ is found from the condition that $(n|_{\nu=1} - n|_{\nu=3})$ exceeds 1 for the first time. Verification of this hypothesis requires a deeper analytical insight than we have at the moment. Moreover, finding a value of $C$ past which the dominant real eigenvalue increases monotonically (as seen in Fig. 9(e)) is also an open question.

# References


[1] R.H. Hardin and F.D. Tappert, Applications of the split-step Fourier method to the numerical soltion of nonlinear and variable coefficient wave equations, SIAM Review (Chronicle) 15 (1973), 423.

[2] G.P. Agrawal, *Nonlinear fiber optics, 3rd Ed.* (Academic Press, San Diego, 2001).

[3] W. Bao and H. Wang, An efficient and spectrally accurate numerical method for computing dynamics of rotating Bose–Einstein condensates, J. Comput. Phys. 217 (2006), 612–626.

[4] A.D. Bandrauk and H. Shen, Exponential split operator methods for solving coupled time-dependent Schrödinger equations, J. Chem. Phys. 99 (1993), 1185–1193.

[5] D. Lanser and J.G. Verwer, Analysis of operator splitting for advection–reaction–diffusion problems from air pollution modelling, J. Comp. Appl. Math. 111 (1999), 201–206.

[6] G. Strang, On the construction and comparison of difference schemes, SIAM J. Numer. Anal. 5 (1968), 506–517.

[7] M. Glassner, D. Yevick, and B. Hermansson, High-order generalized propagation techniques, J. Opt. Soc. Am. B 8 (1991), 413–415.

[8] J.A.C. Weideman and B.M. Herbst, Split-step methods for the solution of the nonlinear Schrödinger equation, SIAM J. Numer. Anal. 23 (1986), 485–507.

[9] A. Carena, V. Curri, R. Gaudino, P. Poggiolini, and S. Benedetto, A time-domain optical transmission system simulation package accounting for nonlinear and polarization-related effects in fiber, IEEE J. Sel. Areas Commun. 15 (1997), 751–764.

[10] Q. Chang, E. Jia, and W. Sun, Difference schemes for solving the generalized nonlinear Schrödinger equation, J. Comp. Phys. 148 (1999), 397–415.

[11] H. Wang, Numerical studies on the split-step finite difference method for nonlinear Schrödinger equations, Appl. Math. Comp. 170 (2005), 17–35.

[12] W. Bao, Q. Tang, and Z. Xu, Numerical methods and comparison for computing dark and bright solitons in the nonlinear Schrödinger equation, J. Comp. Phys. 235 (2013), 423–445.

[13] D. Bambusi, E. Faou, and B. Grébert, Existence and stability of solitons for fully discrete approximations of the nonlinear Schrödinger equation, Numer. Math. 123 (2013), 461–492.

[14] X. Antoine, W. Bao, and C. Besse, Computational methods for the dynamics of the nonlinear Schrödinger/Gross–Pitaevskii equation, Comp. Phys. Commun. 184 (2013), 2621–2633.

[15] W. Bao and Q. Tang, Numerical study of quantized vortex interactions in the nonlinear Schrödinger equation on bounded domains, Multiscale Model. Simul. 12 (2014), 411–439.

[16] G. Li, Recent advances in coherent optical communication, Adv. Opt. Photon. 1 (2009), 279–307.

[17] J. Von Neumann and R.D. Richtmeyer, A method for the numerical calculation of hydrodynamic shocks, J. Appl. Phys. 21 (1950), 232–237.

[18] L.N. Trefethen, *Spectral methods in Matlab* (SIAM, Philadelphia, 2001), Chap. 10.

[19] T.I. Lakoba, Instability analysis of the split-step Fourier method on the background of a soliton of the nonlinear Schrödinger equation, Num. Meth. Part. Diff. Eqs. 28 (2012), 641–669.

[20] D.J. Kaup, Perturbation theory for solitons in optical fibers, Phys. Rev. A 42 (1990), 5689–5694.

[21] H.T. Tran, Stability of dark solitons: Linear analysis, Phys. Rev. A 46 (1992), 7319–7321.

[22] D.E. Pelinovsky, Yu.S. Kivshar, and V.V. Afanasjev, Internal modes of envelope solitons, Physica D 116 (1998), 121–142.

[23] I.M. Gelfand, *Lectures on linear algebra* (Interscience Publishers, New York, 1961), Sec. 15.

[24] G. Chen and J. Zhou, *Vibration and damping in distributed systems, vol. II (WKB and wave methods, vizualization and experimentation)* (CRC Press, Boca Raton, 1993), Sec. 1.2.

[25] S.A. Fulling, Adiabatic expansions of solutions of coupled second-order linear differential equations. II, J. Math. Phys. 20 (1979), 1202–1209.

[26] A.A. Skorupski, Phase integral approximation for coupled ODEs of the Schrödinger type, J. Math. Phys. 49 (2008), 053523.

[27] T. Kapitula and B. Sandstede, Instability mechanism for bright solitary-wave solutions to the cubic-quintic Ginzburg–Landau equation J. Opt. Soc. Am. B 15 (1998), 2757–2762.

[28] J.L. Marin and S. Aubry, Finite size effects on instabilities of discrete breathers, Physica D 119 (1998), 163–174.